

NON-MODAL MECHANISMS IN THE FLOW OVER THE LEADING-EDGE OF BLUNT BODIES

Eduardo Martini

DFTC-2AT

Institut Pprime - CEA

Chasseneuil du Poitou, France

eduardo.martini@univ-poitiers.fr

Clément Caillaud

DFTC-2AT

Institut Pprime - CEA

Chasseneuil du Poitou, France

clement.Caillaud@univ-poitiers.fr

Oliver Schmidt

Dep. of Mech. and Aerospace Eng.

University of California San Diego

California, USA

oschmidt@ucsd.edu

Guillaume Lehnasch

DFTC-2AT

Institut Pprime

Chasseneuil du Poitou, France

guillaume.lehnasch@univ-poitiers.fr

Peter Jordan

DFTC-2AT

Institut Pprime

Chasseneuil du Poitou, France

peter.jordan@univ-poitiers.fr

ABSTRACT

The identification of modal and non-modal mechanisms via stability analysis is an essential component for the prediction of boundary layer transition to turbulence. Here, we use resolvent analysis to study mechanisms that underpins flow streaks in the leading-edge region of an axisymmetric bluff body. Contrary to the receptivity of TS waves, the amplification of zero frequency disturbances is found to increase with the body bluntness, and thus becomes dominant at large bluntness. Compressibility effects are also studied, showing that, for subsonic flows, disturbance amplification increases with the Mach number, with peak amplification occurring at lower azimuthal wavenumbers.

Introduction

Boundary layer (BL) transition can occur via different mechanisms. If external disturbances, such as incoming turbulence, are small, modal mechanisms, in the form of growing instability waves are usually responsible for transition. In incompressible flows, the only unstable mode is the Tollmien-Schlichting (TS) wave. In supersonic flows, at sufficiently high Mach number, there is also a family of unstable modes, understood as acoustic waves trapped in the BL, which were first identified by Mack (1963). The receptivity to acoustic disturbances has been studied both for TS (Goldstein, 1985) and Mack waves (Fedorov & Khokhlov, 1992).

If larger disturbances are present, non-modal mechanisms are often responsible for triggering transition. They are characterized by a transient amplification associated with a linear combination of stable modes, a phenomena known as transient-growth, and which has been characterized for both incompressible (Andersson *et al.*, 1999) and compressible (Hanifi *et al.*, 1996) flows.

Which of the two, modal or non-modal mechanisms, are responsible for transition depends on the amplitude of the incident disturbances and the receptivity of each mechanism. There are several mechanisms by which free-stream disturbances enter the boundary layer. For low turbulence levels, the dominant one is likely localized in the leading edge (Brandt

et al., 2004). The receptivity magnitude will thus provide the initial amplitude of waves involved in modal and non-modal mechanisms. It is also important for scenarios where transition is observed at the leading edge. Due to the strong favourable pressure gradient, which stabilizes TS waves, and the relatively low local Mach number, due to slower velocities and higher temperatures near the stagnation point, transition at the leading edge is believed to be caused by non-modal mechanisms (Paredes *et al.*, 2017). Most studies considering this possibility have been mainly concerned with transition induced by wall roughness.

Aiming to complement previous studies that focused on the receptivity of TS, Mack, and cross-flow instability waves, we here focus on the receptivity of streaks in blunt bodies in non-swept configurations, using a paraboloid body as a test case. A large range of the parameter space was studied, including varying Reynolds and Mach numbers. A description of the method used, results obtained, and their discussion are presented next.

Numerical method

The linearized Navier-Stokes equations can be compactly written as,

$$\frac{\partial q}{\partial t}(\mathbf{x}, t) = Aq(\mathbf{x}, t) + f(\mathbf{x}, t), \quad (1)$$

where q is a vector containing the flow density, velocities, and temperature, and f contain forcing terms. Assuming cylindrical symmetry and using the ansatz

$$q(\mathbf{x}, t) = \hat{q}(z, r)e^{-i\omega t + m\phi}, \quad (2)$$

where r, ϕ , and z are the cylindrical coordinates, (1) is written as

$$(-i\omega - A_m)\hat{q} = \hat{f}, \quad (3)$$

where A_m is the compressible linearized Navier-Stokes operator for the m -th azimuthal component. An input-output relation is obtained re-writing (3) as

$$\hat{q} = R_m(\omega)\hat{f}, \quad (4)$$

where $R_m(\omega) = (i\omega - A)^{-1}$ is the resolvent operator.

A forcing term is said to be optimal if it maximizes the Rayleigh quotient

$$\sigma(\omega) = \frac{\|\hat{q}\|}{\|\hat{f}\|} = \frac{\|R_m(\omega)\hat{f}\|}{\|\hat{f}\|}, \quad (5)$$

where \hat{q} and \hat{f} satisfy (4). The value σ is usually referred as the gain associated with the forcing/response pair. Suboptimal forcing components maximize the same ratio, with the added constraint of being orthogonal to the leading forcing mode.

Gains and forcing/response mode pairs are typically obtained from a singular value decomposition (SVD) of the weighted resolvent operator $R_m'(\omega) = W^{1/2}R_m(\omega)W^{-1/2}$, where W is a matrix representing an energy norm and, for non-uniform meshes, integration weights. However, for two-dimensional systems, the matrix inversion in (3) and the SVD of R_m' become prohibitively costly. Instead, the leading singular values and modes are obtained using an iterative algorithm, such as the power iteration or the Arnoldi algorithms, based on solutions of the linear problem (3). These solutions are typically obtained using an LU decomposition of R_m to reduce the overall cost.

We use a code developed by Schmidt & Rist (2011) to study the modal stability of streamwise corner-flows, which was later extended to non-modal stability analysis (Schmidt & Rist, 2014), and resolvent analysis in Schmidt *et al.* (2018). An important difference with respect to the original code is, that here, the geometry cannot be described by a cartesian mesh, for which the use of finite-differences schemes is most natural. Instead, here an original rectangular domain, described by the coordinates ξ_i , is mapped onto the desired geometry, resulting in curvilinear coordinates $x_j = x_j(\xi_i)$. The mapping is illustrated in figure 1.

In order to model the system in the physical domain (x_j), differentiation matrices need to be constructed based on the finite differences used in the original domain (ξ_i). First order derivatives with respect to x_j are obtained from the derivatives in the original domain as

$$\partial_{x_i}g = J_{ij}^{-1}\partial_{\xi_j}g, \quad (6)$$

where $J_{ij} = \partial x_j / \partial \xi_i$ represents the mapping Jacobian, g is a scalar field, and the Einstein summation convention is used. The Jacobian \mathbf{J} is computed numerically and then inverted to obtain \mathbf{J}^{-1} .

Second derivatives can be obtained by re-applying (6). However, when using this approach the effective stencil for second derivatives doubles, which is an undesirable feature when used to numerically construct the operator A_m , as it becomes less sparse, increasing the computational cost. Instead,

second derivatives are computed as

$$\begin{aligned} \partial_{x_i}\partial_{x_j}g &= \partial_{x_i}\left(J_{jq}^{-1}\partial_{\xi_p}g\right) \\ &= \left(\partial_{x_i}J_{jp}^{-1}\right)\partial_{\xi_p}g + J_{jp}^{-1}\left(\partial_{x_i}\partial_{\xi_p}g\right) \\ &= \left(\partial_{x_i}J_{jp}^{-1}\right)\partial_{\xi_p}g + J_{jp}^{-1}J_{iq}^{-1}\partial_{\xi_q}\partial_{\xi_j}g, \end{aligned} \quad (7)$$

where $\partial_{x_i}J_{jp}^{-1}$ is computed using the matrix identity

$$\partial_{x_i}\mathbf{J}^{-1} = -\mathbf{J}^{-1}\left(\partial_{x_i}\mathbf{J}\right)\mathbf{J}^{-1}. \quad (8)$$

The term $\partial_{x_i}\mathbf{J}$ contains information about the second derivatives of the mapping, and reads

$$\partial_{x_i}J_{jk} = \frac{\partial^2 x_j}{\partial x_i \partial \xi_k} = J_{im}^{-1} \frac{\partial^2 x_j}{\partial \xi_m \partial \xi_k}. \quad (9)$$

This term is also computed numerically.

With this formulation, the effects of the mapping is computed explicitly, and the differentiation matrix retains its sparsity.

Throughout this work, a 4-th order differentiation scheme is used to numerically compute the derivatives, using a centered scheme in the interior the domain and biased stencils on the boundaries.

Geometry and baseflow

The body surface is given by

$$x = (z^2 + y^2) - 1/4. \quad (10)$$

The free-stream flow moves towards $+z$ with unit velocity. The problem is made non-dimensional with respect to the freestream density, viscosity and velocity and the diameter of curvature of the leading edge.

The inviscid and incompressible flow around the body is obtained analytically using parabolic coordinates, (σ, τ, ϕ) , given by

$$z + ir = (\sigma + i\tau)^2, \quad (11)$$

$$r = \sqrt{(x^2 + y^2)}, \quad (12)$$

$$\phi = \tan^{-1}(y/x). \quad (13)$$

The body surface corresponds to $\sigma = \sigma_0 = -1/2$, and the cylindrical coordinates are recovered as $z = \sigma^2 - \tau^2$ and $r = 2\tau\sigma$. The flow potential function, ψ , is given by the solution of the Laplace equation,

$$\nabla_{\sigma, \tau, \phi}^2 \psi = \frac{1}{\sigma} \frac{\partial}{\partial \sigma} \left(\sigma \frac{\partial \psi}{\partial \sigma} \right) + \frac{1}{\tau} \frac{\partial}{\partial \tau} \left(\tau \frac{\partial \psi}{\partial \tau} \right) + \frac{\partial^2 \psi}{\partial \phi^2}, \quad (14)$$

with no penetration boundary condition at the body surface, $\frac{\partial \psi}{\partial \sigma} = 0$ for $\sigma = \sigma_0$, and the requirement that far from the body

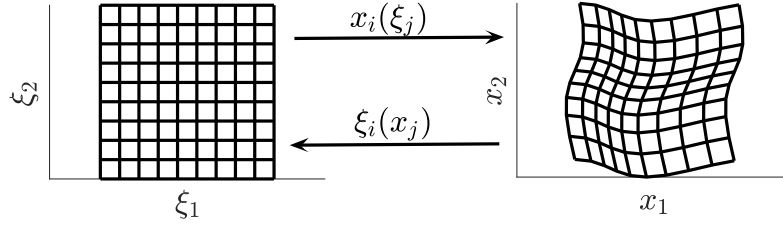


Figure 1: Illustration of mapping between the original (ξ_i) and desired (x_i) meshes.

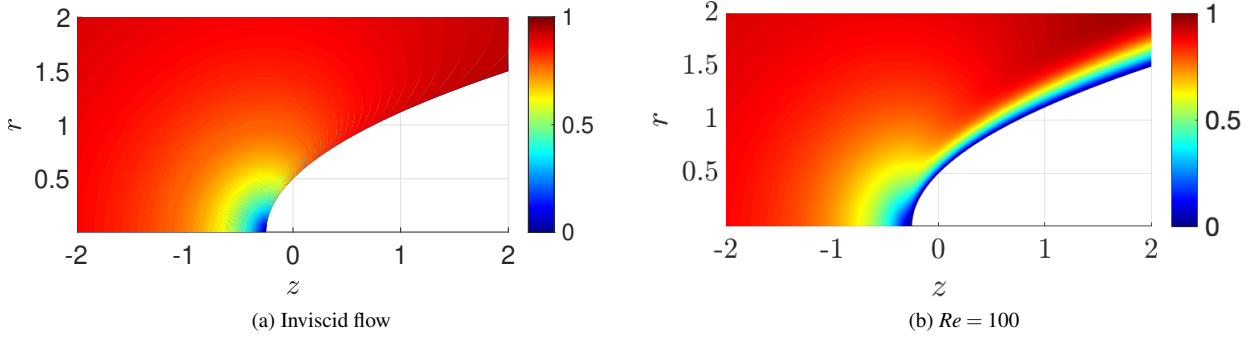


Figure 2: Velocity magnitude of the baseflow for the inviscid and $Re = 100$ incompressible flows. Base flows for the compressible cases are qualitatively similar, with an increase in temperature, density and viscosity in the regions of low flow velocity, i.e., the stagnation point and in the boundary layer.

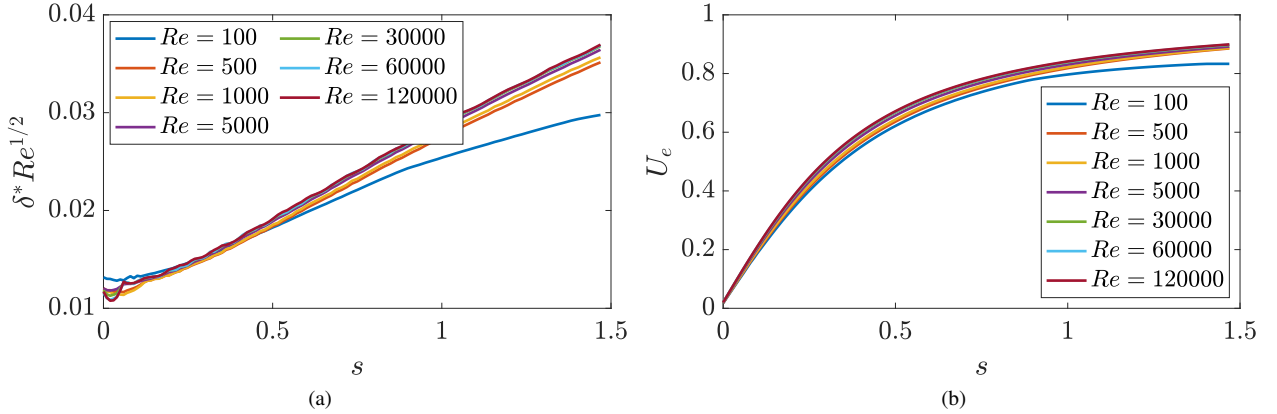


Figure 3: Boundary layer displacement thickness (a) and edge velocity (b).

to flow corresponds to a uniform right-moving flow, i.e. $\psi = z = (\sigma^2 - \tau^2)$ at $\sigma \rightarrow \infty$. The solution is given by

$$\psi = \sigma^2 - \tau^2 + 2\sigma_0^2 \log(\sigma). \quad (15)$$

From (15), the influence of the paraboloid body on the flow scales decays roughly with the logarithm of the wall distance. Accurately capturing this effect numerically would require a large computational domain if uniform free-stream boundary conditions were used as inflow of a viscous incompressible simulation domain. To reduce the required computational domain needed, the inviscid solution was thus used as a boundary condition for the viscous problem.

Viscous incompressible baseflows were obtained by time-marching the incompressible Navier-stokes equations in time until the norm of the velocity time-derivative becomes smaller

than 10^{-8} . No-slip boundary conditions were applied at the body surface and outflow conditions on the right-most edge of the domain. Integration was carried out using the axisymmetric formulation of the spectral code Nek5000 (Fischer & Lottes, 2005). The inviscid and the $Re = 100$ baseflows are shown in figure 2. The baseflows for higher values of Re look similar, but with thinner boundary layers. The computational domain and mesh discretization used to obtain the baseflows for each Reynolds number were chosen to guarantee a domain considerably larger than the boundary layer around the body and to have sufficient grid points inside it.

The boundary layer displacement thickness (δ^*) and boundary layer edge velocities (U_e) as a function of the distance to the leading edge and the Reynolds number is presented in figure 3. The BL thickness for $Re > 5000$ is seen to scale with $Re^{-1/2}$, as typically observed for flat plates. The

solution at the boundary layer edge closely follows the inviscid solution at the surface and is nearly independent of the Reynolds number

Reynolds number effects

To study the effect of the Reynolds number on the leading forcing/response modes close to the stagnation point, the physical domain was initially limited downstream to $z = 1$. As will be soon reported, the forcing mode extends further upstream for increasing Reynolds numbers, and thus the upstream boundary has been moved further from the body for larger values of Re . An extended domain, truncated at $z = 2$, was used to verify the impact of the domain truncation.

Figure 4a shows the gains of the optimal forcing/response pair as a function of Reynolds number and the azimuthal mode. Figure 4b shows that maximum gains and their azimuthal wave numbers increase with the Reynolds number. Figure 4c shows that the same gain and azimuthal wavenumber trends are observed when the domain is increased, although at higher nominal values. To explore these trends, we first illustrate the structure of forcing and response modes.

Figure 5 shows the leading forcing and response modes for the flow with $Re = 60000$ and azimuthal number $m = 26$. The forcing mode is mainly located upstream of the body and mainly generates vortical disturbances aligned in the radial direction, while the response is concentrated on the thin boundary layer, where the velocity perturbations are aligned with the base flow.

The dynamics of the system can be described as follows: radially-aligned vortical disturbances are generated upstream of the body and are convected into the BL close to the stagnation point. Once in the boundary layer, these vortical disturbances are aligned with the base flow, as, near the stagnation point, the velocity profile of the boundary layer is mainly radial, and thus triggers the lift-up mechanism which generates wall-aligned streaks. The trend of the forcing mode having negligible azimuthal components was observed for all Reynolds numbers at the peak azimuthal mode.

The sub-optimal modes are shown in figure 6. Their structure is analogous, with sub-optimal modes showing radial oscillations in the forcing components, and amplifications 3 to 5 times lower.

The basic mechanism for all Reynolds numbers remains approximately the same, with minor variations. Figure 7 shows the forcing energy for the leading mode for different Reynolds numbers. If, on one hand, it could be expected that an increase in the Reynolds number would lead to an upstream extension of the forcing support, as the lower dissipation levels may favour a spreading of the forcing terms, on the other, higher azimuthal wave number reduces the distance between vortical disturbances in the azimuthal direction, increasing shear and thus dissipation. These two trends seem to partially compensate for each other, and the forcing domain remains approximately the same. One notable difference is that for higher Reynolds numbers the forcing mode slightly approaches the $r = 0$ axis. This can be interpreted as perturbations impinging closer to the stagnation to penetrate the thinner BLs.

Compressibility effects

In order to investigate the influence of compressibility on the lift-up mechanism, baseflows for Mach numbers 0.3, 0.6 and 0.9 were obtained using the SU2 code (Economou *et al.*, 2016). Figure 8 shows the leading gains for these conditions

using Chu's and the kinetic energy norms. In the latter, only forcing associated with the momentum equations and flow velocities are used in the norm.

Gains obtained using Chu's energy norm are higher than those obtained using only the kinetic energy norm. For the Mach 0.3 and Mach 0.6 cases, the gains obtained with the kinetic energy norm are approximately the same as those obtained with Chu's norm for a lower Mach number. In particular, this suggests that the main effect of compressibility for Mach numbers up to 0.3 is to couple the perturbations of density and temperature to those of velocities, with negligible influence of the baseflow. The preferred azimuthal number is not affected by compressibility for Mach numbers up to 0.6.

For the Mach 0.9, a larger discrepancy is observed, and the optimal disturbances are found at a lower azimuthal number. The difference cannot be attributed to local variations in viscosity, as at the stagnation point it increases only by $\approx 15\%$, and thus is likely due to more complex phenomena, possibly related to density variation, which is 40% greater at the stagnation point than on the freestream.

Conclusions

Non-normal mechanisms for perturbation amplification near an axisymmetric leading edge of the blunt body were studied. Using a model paraboloid body, identification of leading forcing and response modes reveals that the lift-up mechanism is optimally excited upstream of the body, creating vortical disturbances that are convected into the boundary layer at the stagnation point. This mechanism is different from those studied by Andersson *et al.* (2001), where streamwise vortical disturbances are generated directly inside the boundary layer, and Brandt *et al.* (2004), where it is excited by non-linear interactions of the free-stream turbulence, and that of Paredes *et al.* (2017), where optimal perturbations inside the boundary layer are computed, which could be excited by wall roughness elements.

The scaling of the optimal gain and associated azimuthal number found in this study contrasts with those found on developed flat-plate boundary layers. On the latter, optimal gains are seen to scale with $Re \propto Re_{\delta^*}^2$, and the spanwise wavelength is proportional to the BL thickness. On the paraboloid body, the gains are found to scale with $Re^{1/2} \propto Re_{\delta^*}$, thus showing a considerably slower growth with Re . The azimuthal wavenumber, which for a given position at the body is inversely proportional to the spanwise wavelength, scales with $Re^{1/4} \propto \delta^{*1/2}$.

The lower gains are explained by the domain truncation: in developed boundary layers the streamwise streaks are continuously forced by vortical disturbances. Both these structures are damped by viscosity at a rate of Re^{-1} , and thus have a total length $\propto Re$. For larger Re vortical disturbances excite the streaks via the lift-up mechanisms for a longer time, resulting in the classical Re^2 gain scaling. The finite domain used here reduces the efficacy of the lift-up mechanism, and thus reducing the overall gain. This suggests that leading edge transition, for which the relevant dynamics necessarily occurs in a short distance, will exhibit this slower scaling with respect to Re and/or free-stream turbulent intensity. The relatively low magnitude of the gains can be explained by two different mechanisms. The first one is the flow curvature, which pushes fast streaks away from the body and slow streaks closer to it, counteracting the generated vortical disturbances. This mechanism stabilizes the flow, which should further reduce the gains. The second is the radial evolution of the boundary layer. The conservation of the azimuthal wavenumber, as opposed to that of

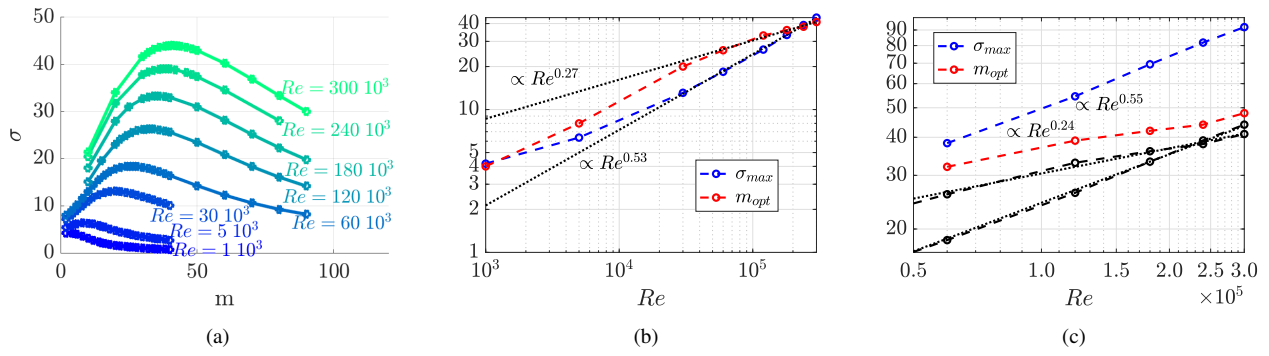


Figure 4: Optimal gains for different Reynolds numbers and azimuthal numbers for the small domain (a), and trends observed in the peak values with Reynolds numbers (b). In (c), the trends found for the extended domain are presented, with data from (b) added in black for reference.

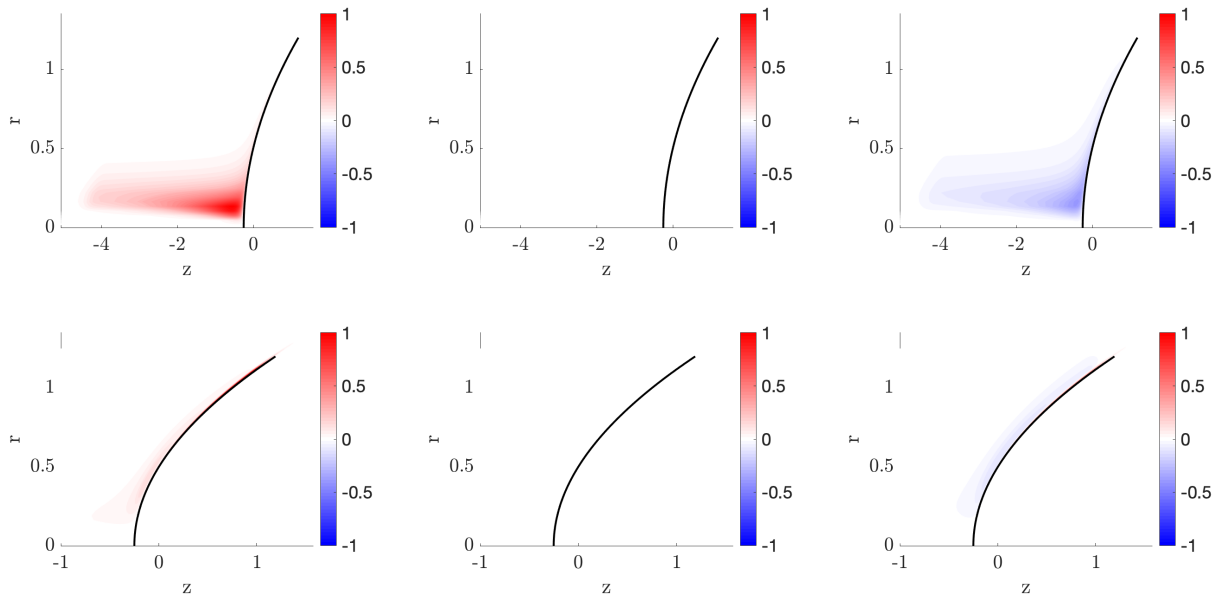


Figure 5: Forcing (top) and response (bottom) modes for $Re = 60000$ and $m = 26$. The responses in the axial, azimuthal and radial directions, and the corresponding forcing components, are shown from left to right. The radial, azimuthal and axial directions contain 84%, 1% and 15% of the forcing energy, and 71%, 7% and 23% of the response energy, respectively.

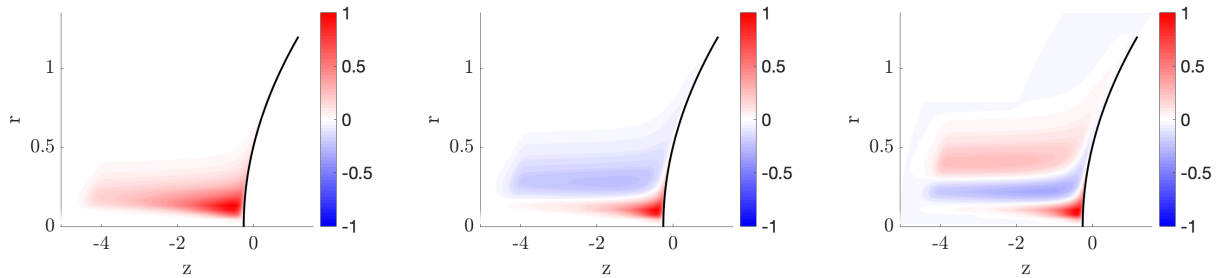


Figure 6: Optimal and suboptimal forcing modes for $Re = 60000$. Only the radial forcing component is shown for brevity. The computational domain used is insufficient to converge the rightmost mode, due to its larger radial structure. However, as the suboptimal modes have considerably lower gains, no effort to properly converge them was carried out.

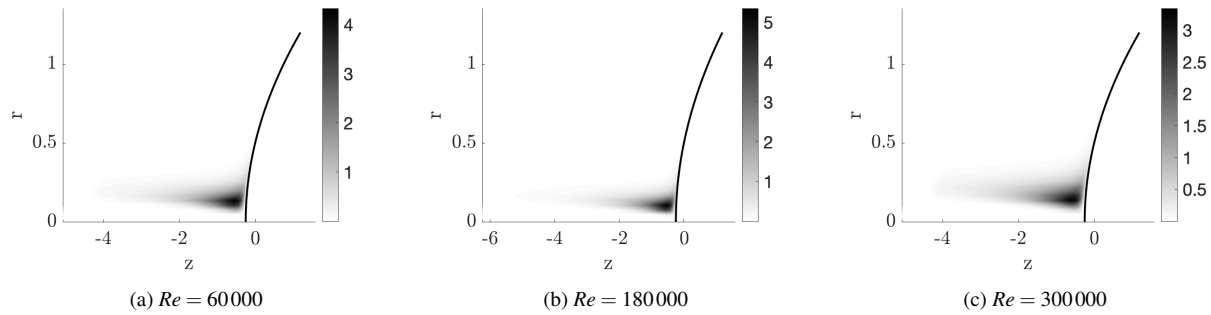


Figure 7: Forcing energy density for the optimal azimuthal wavenumbers at different Reynolds numbers. The plots are normalized as to have unit energy.

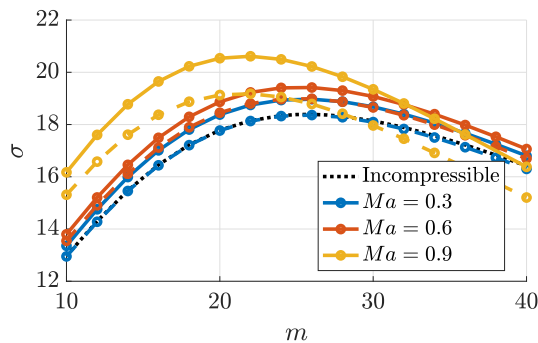


Figure 8: Gains using Chu's (solid) and kinetic energy (dashed) norms for $Re = 60\,000$ and different Mach numbers.

the span-wise wavenumber in the flat-plate case, means that a given mode has different spanwise lengths at each body location. Thus, the length, measured in boundary layer thicknesses, that maximizes the lift-up effect can only be attained at specific locations. Although this is also the case in spatially evolving boundary layers, the evolution of the BL thickness is usually small, contrasting with the evolution of the paraboloid body radius, which varies very fast near the leading edge.

Finally, compressibility effects for subsonic flows were investigated. It is observed that compressibility increases perturbations amplification and reduces the optimal azimuthal wavenumber when the flow approaches sonic speeds.

Acknowledgements

This work is part of the project TRANSITION supported by Région Nouvelle Aquitaine under grant 2018- 1R10220. Additionally, this work was granted access to the HPC resources of IDRIS under the allocations 2020-A0092A10868 and 2021-A0112A10868 made by GENCI.

REFERENCES

Andersson, Paul, Berggren, Martin & Henningson, Dan S. 1999 Optimal disturbances and bypass transition in boundary layers. *Physics of Fluids* **11** (1), 134–150.

- Andersson, Paul, Brandt, Luca, Bottaro, Alessandro & Henningson, Dan S. 2001 On the breakdown of boundary layer streaks. *Journal of Fluid Mechanics* **428**, 29–60.
- Brandt, Luca, Schlatter, Philipp & Henningson, Dan S. 2004 Transition in boundary layers subject to free-stream turbulence. *Journal of Fluid Mechanics* **517**, 167–198.
- Economou, Thomas D., Palacios, Francisco, Copeland, Sean R., Lukaczyk, Trent W. & Alonso, Juan J. 2016 SU2: An Open-Source Suite for Multiphysics Simulation and Design. *AIAA Journal* **54** (3), 828–846.
- Fedorov, A. V. & Khokhlov, A. P. 1992 Excitation of unstable modes in a supersonic boundary layer by acoustic waves. *Fluid Dynamics* **26** (4), 531–537.
- Fischer, Paul F. & Lottes, James W. 2005 Hybrid Schwarz-Multigrid Methods for the Spectral Element Method: Extensions to Navier-Stokes. In *Domain Decomposition Methods in Science and Engineering* (ed. Timothy J. Barth, Michael Griebel, David E. Keyes, Risto M. Nieminen, Dirk Roose, Tamar Schlick, Ralf Kornhuber, Ronald Hoppe, Jacques Périaux, Olivier Pironneau, Olof Widlund & Jinchao Xu), vol. 40, pp. 35–49. Berlin/Heidelberg: Springer-Verlag.
- Goldstein, M. E. 1985 Scattering of acoustic waves into Tollmien-Schlichting waves by small streamwise variations in surface geometry. *Journal of Fluid Mechanics* **154**, 509–529.
- Hanifi, Ardeshir, Schmid, Peter J. & Henningson, Dan S. 1996 Transient growth in compressible boundary layer flow. *Physics of Fluids* **8** (3), 826–837.
- Mack, LM 1963 The stability of the compressible laminar boundary layer according to a direct numerical solution. Part IV. *Space Programs Summary* **37**, 24.
- Paredes, Pedro, Choudhari, Meelan M. & Li, Fei 2017 Blunt-body paradox and transient growth on a hypersonic spherical forebody. *Physical Review Fluids* **2** (5), 053903.
- Schmidt, Oliver T. & Rist, Ulrich 2011 Linear stability of compressible flow in a streamwise corner. *Journal of Fluid Mechanics* **688**, 569–590.
- Schmidt, Oliver T. & Rist, Ulrich 2014 Viscid–inviscid pseudo-resonance in streamwise corner flow. *Journal of Fluid Mechanics* **743**, 327–357.
- Schmidt, Oliver T., Towne, Aaron, Rigas, Georgios, Colonius, Tim & Brès, Guillaume A 2018 Spectral analysis of jet turbulence. *Journal of Fluid Mechanics* **855**, 953–982.